Journal of Materials Chemistry A

Hierarchical Polyaromatic Hydrocarbons (PAH) with Superior Sodium Storage Properties

Journal:	*Journal of Materials Chemistry A*
Manuscript ID	TA-ART-04-2021-003101.R1
Article Type:	Paper
Date Submitted by the Author:	27-Jun-2021
Complete List of Authors:	Qu, Jie; Southern University of Science and Technology, Shenzhen Key Laboratory of Solid-State Batteries; Southern University of Science and Technology, Department of Materials Science and Engineering; Southern University of Science and Technology, Guangdong Provincial Key Laboratory of Energy Materials for Electric Power Dai, XinXin; Southern University of Science and Technology, Department of Materials Science and Engineering Cui, Jieshun; Southern University of Science and Technology, Department of Materials Science and Engineering Wang, Xin; Southern University of Science and Technology, Academy for Advanced Interdisciplinary Studies & Department of Physics Chen, Rouxi; Southern University of Science and Technology, Department of Materials Science and Engineering Lin, Yen-Hao; Rice University, Department of Chemical and Biomolecular Engineering Verduzco, Rafael; Rice University, Chemical and Biomolecular Engineering Wang, Hsing-Lin; Southern University of Science and Technology, Shenzhen Key Laboratory of Solid State Batteries; Southern University of Science and Technology, Department of Materials Science and Engineering; Southern University of Science and Technology, Guangdong Provincial Key Laboratory of Energy Materials for Electric Power

Hierarchical Polyaromatic Hydrocarbons (PAH) with Superior Sodium Storage Properties

Jie Qu[a,b,c], Xin-Xin Dai[b], Jie-Shun Cui[b], Rou-Xi Chen[b], Xin Wang[d], Yen-Hao Lin[e], Rafael Verduzco[e], Hsing-Lin Wang[a,b,c,*]

a.   *Shenzhen Key Laboratory of Solid State Batteries, Southern University of Science and Technology, Shenzhen 518055, China*
b.   *Department of Materials Science and Engineering, Southern University of Science and Technology, Shenzhen, 518055, China.*
c.   *Guangdong Provincial Key Laboratory of Energy Materials for Electric Power, Southern University of Science and Technology, Shenzhen 518055, China*
d.   *Academy for Advanced Interdisciplinary Studies & Department of Physics, Southern University of Science and Technology, Shenzhen, Guangdong, 518055, China*
e.   *Department of Chemical and Biomolecular Engineering, Rice University, Houston TX, 77005, United States.*

Abstract

Designing a structurally stable anode with a high reversible capacity for sodium ion batteries (SIBs) is particularly crucial to meet the large-scale application in grid electrical energy storage. Organic molecule Polyaromatic Hydrocarbons (PAHs) with well-defined structure show excellent performance in lithium storage. Based on our well-established correlation between battery property and molecular structure, a recently synthesized Hexabenzocoronene (HBC) and corresponding derivate HBC-OMe was firstly applied in sodium storage. HBC molecule forms self-assemblies which has long-range ordered face-center cubed (fcc) structure due to the interaction between two HBC moieties. Such unique 3D structure is expected to generate a strong π–π interaction between flakes and thus yield amazing durability during long-term cycling

process. In addition, the surface-dominated Na^+ storage mechanism could facilitate the Na^+ transport kinetic and alleviate the structural strain during charging-discharging cycles simultaneously. Benefiting from the coupling effect of surface-driven capacitive process and the robust 3D self-assembled hierarchical nature, oxygen-contained sample HBC-OMe shows extraordinary sodium storage capability, which attains a high capacity of 506 mAh g^{-1} at 0.1 A g^{-1}, excellent rate capability (217 mAh g^{-1} at 5 A g^{-1}) and superior long-term cycling performance (290 mAh g^{-1} at 2 A g^{-1} with negligible capacity fade after 1000 cycles).

Keywords: Sodium-ion batteries, Self-assembled structure, Anode materials, Electrochemistry.

1. Introduction

With the foremost commercialization of Lithium Ion Batterie (LIBs) by Sony in the early 1990s, the excellent electrochemical performances of LIBs have made it into a primary power source of mobile electronic devices and hybrid electric vehicles, which significantly alleviated the energy shortage and environmental problems.[1] However, the high cost and geographically-limited distribution of lithium element seriously impeded the utilization of LIBs in large-scale energy storage system (ESS).[2-4] Accordingly, the exploration of next generation rechargeable batteries such as sodium ion, magnesium ion, aluminum ion batteries are of great interest due to potential high charge capacity and stability. In particular, due to the low cost and widely distributed sodium resources, SIBs have been regarded as the most promising alternative for

LIBs.[5-17]

Nevertheless, compared with Li$^+$, the larger ionic radius of Na$^+$ (1.02 Å) leads to a greater volume expansion and structure transformation during Na$^+$ intercalation processes. Additionally, the heavier atomic weight of Na and higher electrochemical standard potential of Na$^+$/Na result in lower gravimetric/volumetric densities compared with that of LIBs. Therefore, developing advanced anode materials with low working potential and excellent structural stability is an effective way to enhance the energy densities for SIBs.

Among all types of anode materials for SIBs, graphene is becoming increasingly popular owing to the excellent physical/chemical properties such as high mechanical strength, electronic conductivity and a large specific surface area. However, the pristine graphene sheets for SIBs do not deliver decent reversible capacity due to the relatively narrow interlayer space for Na$^+$ intercalation.[18-20] Structural modification has been attempted to enlarge the *d*-spacing between pristine graphene sheets. Chang's group used a modified Staudenmaier method to successfully synthesize graphene nanosheets and increased the interlayer spacing to 0.375 nm, which apparently improved its reversible capacity.[21] Ma's group proposed a novel selective etching method to successfully synthesize co-doped holey graphene aerogel and enlarged its intercalation distance to 0.38 nm.[18] Although these modified graphene materials have a relatively larger interlayer distance and improved device performances, there is ample space to optimize Na$^+$ storage capability for anode electrodes in SIBs. In addition, another

obstacle impeding the further improvement is the unsatisfied cycling performance owing to the restacking of graphene layers during the Na$^+$ intercalation processes, which also occurred among 1D/2D graphene materials such as nanoribbons or nanosheets.[22,23]

Thus, we should search for a more robust self-assembled structure to replace traditional graphene materials for SIBs. Polycyclic aromatic hydrocarbons (PAHs), assemblies ranging from 1 nm to 100 nm composed of *SP²*-hybridized carbon atoms, have physical/chemical properties similar to that of traditional graphene materials.[24,25] Despite a large expanded π–π interaction of PAHs, the well-defined molecular structure of PAHs could help us better understand the correlation between structure and property. Among all types of PAHs, Hexabenzocoronene (HBC) is the smallest nano assemblies in size,[26] which are aromatic organic molecules comprised of *SP²*-hybridized carbon atoms and is beneficial to the contact between the electrolyte and sodium and thus facilitate the desodiation and sodiation processes. As shown in **Figure 1**, HBC owns a propeller-shaped structure which is composed of center *SP³*-hybridized nitrogen and three flakes, it can form long-range ordered self-assemblies with a face-center cubed (fcc) structure. Such unique 3D self-assembled structure could not only yield an ultrahigh long-term structure stability during prolonged charging-discharging processes, but also provide an impressive larger *d*-spacing for Na$^+$ intercalation and thus possess excellent rate performance compared with traditional modified graphene materials.
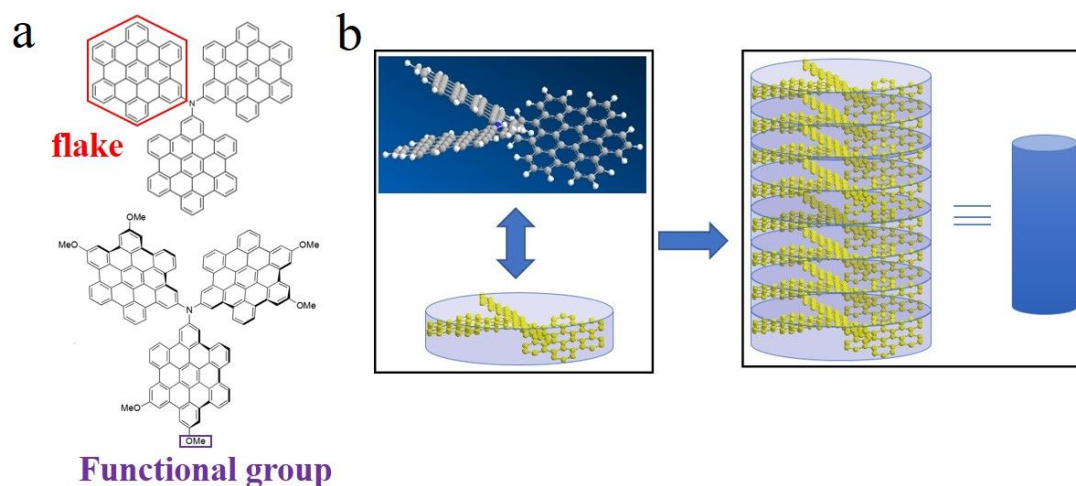
Figure 1. Organic chemical structures of HBC and HBC-OMe (a), Schematic diagram of self-assembled structure (b).

In this work, we employ a newly synthesized HBC for sodium storage. Controlled organic synthesis allows us to precisely tune the molecular structure and provide a clear elucidation between the battery property and molecular structure. We have also shown that a series of PAH derivatives have been synthesized and the structure-property correlation has been clearly established.[27] In order to further explore the influence of molecular structure and sodium storage capacity of PAH, we use the HBC-OMe derivative and compared its structure details, electrochemical performances with pristine HBC. The cyclic voltammetry results indicate that the charge capacity is mainly originated from the surface adsorption/desorption process at high scan rate. Such surface-dominated Na^+ storage mechanism can not only facilitate the Na^+ transport kinetic but also alleviate the structural strain during Na^+ intercalation process. There are two Na^+ storage mechanisms for HBC and HBC-OMe electrode, which are intercalation process and surface adsorption/desorption process, respectively. Sodium

can intercalate into the available space between the carbon layers or can be adsorbed on the carbon surface and complex with the oxygen in the methoxyl functional groups[28]. Moreover, previous studies also reveal the edge of the nanographene structure with zigzag and arm chair configuration can interact with Li ions that play a significant role in the enhancement of charge capacity[29,30]. Our 2D X-ray further validates that the HBC forms self-assemblies with long range order consistent with a face-center cubed (fcc) structure, resulting from interaction between two HBC moieties. Benefiting from the coupling effect of surface-induced capacitive process and the robust 3D self-assembled hierarchical structure, the as-prepared HBC-OMe sample shows extraordinary electrochemical performances, attaining a high capacity of 506 mAh g^{-1} at 0.1 A g^{-1}, brilliant rate capability (217 mAh g^{-1} at 5 A g^{-1}) and excellent long-term cycling durability (291 mAh g^{-1} at 2 A g^{-1} and capacity retention close to 100% after 1000 cycles).

2. Experimental Section

2.1 Material preparation

Detailed synthesis of HBC and HBC-OMe has been published in our previous work,[27] the major procedures are shown in Supporting Information.

2.2 Electrochemical Measurements

The electrochemical performances of as-prepared samples were tested in CR2025 coin cells. These cells were assembled in the highly argon-filled glove box in which the water and oxygen partial pressure was kept below 0.1 ppm. The anode comprised of

active materials, Ketjen Black and polyvinylidene fluoride (PVDF) with a mass ratio

of 75: 15: 10. After fully mixing for several minutes, an appropriate amount of N-

methyl- 2-pyrrolidone (NMP) was added in the mixed powder to form an even slurry.

Then, the slurry was evenly casted on copper foils, which would be subsequently put

into the vacuum oven for 12 hours at 80 °C. The pure Na metal and glass fiber (GF/D

Whatman) was used as cathode and separator, respectively. The electrolyte was 1 mol

L^{-1} $NaPF_6$ and a mixture of EC and DEC at a volume ratio of 1: 1 with 2 vol% FEC

additive. The galvanostatic charge–discharge tests including cycling capability and rate

performances were measured on the Neware BTS-610 battery tester at a voltage scope

of 0.01–3.0 V. Electrode kinetics performances were obtained by the technique of

Electrochemical Impedance Spectroscopy (EIS). The EIS measurements were

performed on a Zahner electrochemical workstation with an applied alternating current

amplitude of 5 mV.

2.3 Material Characterization:

The structures of as-prepared samples were measured by X-ray diffraction (XRD, Cu

Kα radiation, λ=1.54056 Å, Bruker D8 Advance) analysis. Scanning electron

microscopy (SEM, TESCAM MIRA3) was applied to characterize the powder samples'

morphologies. Detailed crystal lattice of primary particles was investigated by high-

resolution transmission electron microscopy (HRTEM FEI Tecnai G2 F30). The

Raman spectra were obtained by using a LabRAMHR800UV spectrometer. High-

resolution X-ray photoelectron spectroscopy (XPS, Thermo ESCALAB 250Xi) was

applied to investigate the C and O distribution of as-prepared sample. 2D X-ray is carried out for HBC to reveal long-range order resulting from self-assemblies. The porosity and Brunauer–Emmett–Teller (BET) surface area analysis was performed using an ASAP 2460 (micromeritics, USA) gas sorption analyzer. Both samples were outgassed (activated) at 100 °C for 12 hours.

2.4 Grazing-Incidence X-ray Scattering Measurements.

Grazing incidence Small-Angle X-ray scattering (GISAXS) measurements were carried out on Sector 8 at the Advanced Photon Source, Argonne National Laboratory. Beamline 8-ID-E operates at an energy of 7.35 keV, and images were collected from a Pilatus 1MF camera (Dectris), with two exposures for different vertical position of the detector. After flat-field correction for detector nonuniformity, the images are combined to fill in the gaps for rows at the borders between modules, leaving dark only the columns of inactive pixels at the center. Using the GIXSGUI package for MATLAB (MathWorks), data are corrected for X-ray polarization, detector sensitivity, and geometrical solid angle. The beam size was 200 μm (h) × 20 μm (v), and the sample–detector distance was 204 mm. Sample measurement and thermal annealing were carried out under vacuum, with the sample stage interfaced with a Lake Shore 340 unit.

3. Results and Discussion

The XRD patterns of HBC and HBC-OMe are displayed in **Figure 2a**. Broad peaks located at 22.5° and 44.3° can be seen in each sample, corresponding to the (002) diffraction resulted from the graphitic layered structure and graphite-induced (100)

diffraction, respectively.[31] Both HBC and HBC-OMe sample do not show high crystallinity, which corresponds to the mostly inconsecutive and irregular lattices. The fitted Raman spectra of HBC and HBC-OMe are presented in **Figure 2b**. Both the D and G bands could be clearly observed in as-prepared samples, which corresponds to the imperfect sp^2 carbon bonding and phonon vibration of well-ordered graphite, respectively. The unfitted Raman spectra is shown in Figure S1. Compared with the fitted spectra, the pristine one displays apparent noisy peaks which is resulted from the interface of testing environment. Interestingly, there are two peaks of D band for HBC sample, which are ascribed to the ring breathing modes of HBC[32].The HBC-OMe sample exhibits higher peak intensity ratio of the D to G band ($I_D/I_G = 0.82$) compared with that of HBC sample ($I_D/I_G = 0.6$),[33] which implies that the introduction of functional group could accelerate the structural disorderliness and defectiveness and thus could be more conductive to promote the Na^+ diffusion. XPS was carries out to investigate the C and O elements distribution of HBC and HBC-OMe samples. The results are shown in **Figure 2c**, where a strong C1s peak and a weak N1s peak presented at ~ 284.8 eV and ~399.7 eV, respectively, in both HBC and HBC-OMe samples. Importantly, O element could not be noticed in HBC spectrum, which conforms its chemical formula. In comparison, a noticeable O1s appears in HBC-OMe sample, which is originated from the introduction of oxygen-containing functional group. As displayed in **Figure 2d**, the O content increased to 16.23% in HBC-OMe sample. The elemental composition data are shown in **Table S1**. The porous character of the

activated samples of HBC and HBC-OMe were revealed in N_2 sorption experiments (at

77 K). A typical type-I gas adsorption isotherm (Figure S2) was observed in HBC

sample, with a BET surface area of 574 m^2/g. The pore size distribution of HBC sample

indicated an average pore width of 3.43 nm, with a pore volume of 0.27 cm^3/g.

Meanwhile, a typical type-II gas adsorption isotherm was observed in HBC-OMe

sample, with a BET surface area of 39 m^2/g. The pore size distribution of HBC-OMe

sample indicated an average pore width of 15.85 nm, with a pore volume of 0.12 cm^3/g.

Compared to HBC, the decrease of surface area of HBC-OMe may be attributed to the

introduced methoxy group, which lead to its packing disorder.
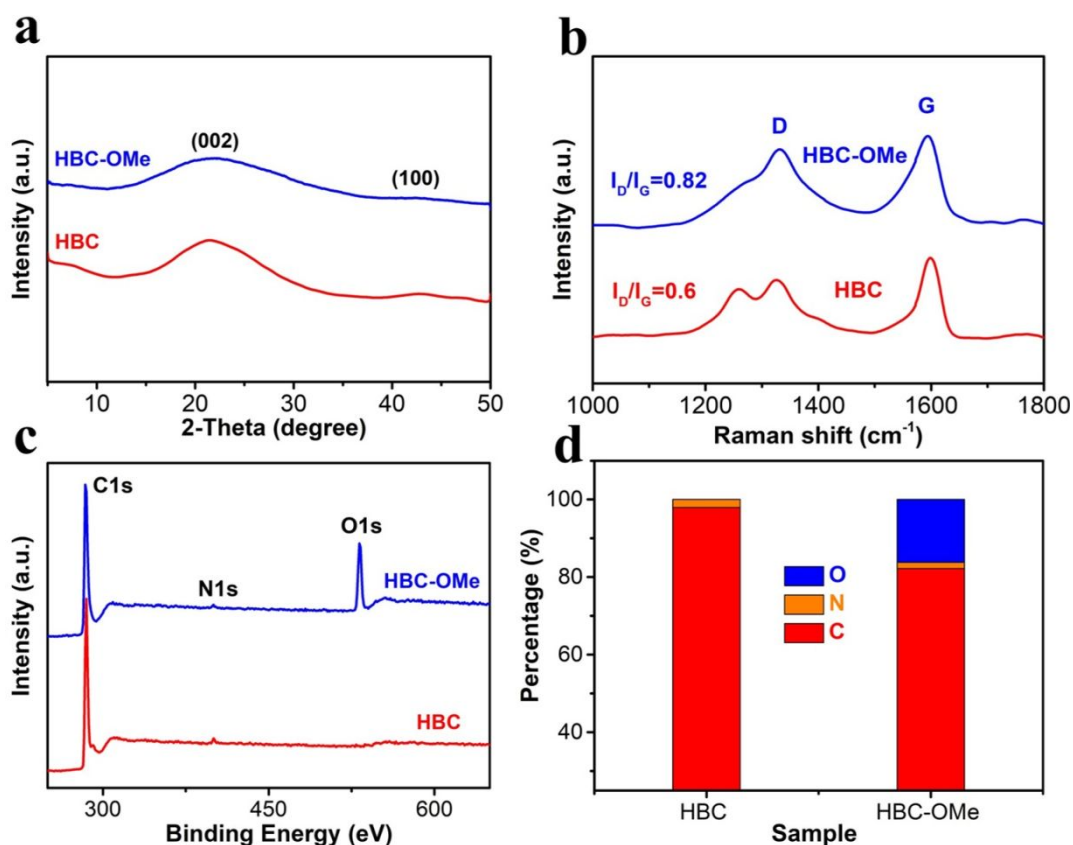
Figure 2. Microstructure measurements of as-prepared samples: (a) XRD patterns, (b) Raman spectrum, (c) High-resolution wide-range XPS spectra and (d) percentage of C and O element ratio in different samples.

Quantitative analysis of X-ray data is a significant way to fundamentally investigate the structure/property relationship in energy storage materials. Grazing incidence small-angle X-ray scattering (GISAXS) analysis for HBC was used to identify the nature of self-assembled structure.[34] As shown in **Figure 3a**, the GISAXS measurements revealed a series of diffraction peaks aligned perpendicular to the surface normal, demonstrating alignment and crystallinity of the HBC-OMe sample. The corresponding intersity-q_z profile and *d*-space plane distribution are shown in **Figure 3b**, which reveals the long-range ordered self-assembled structure.
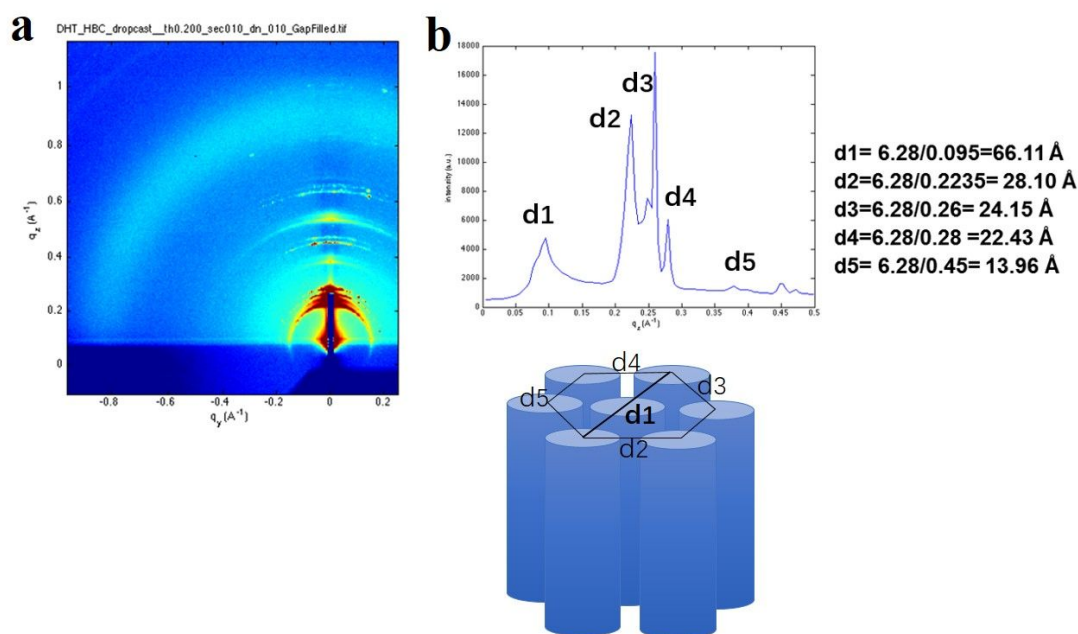
Figure 3. 2D X-ray data. Grazing incidence small-angle X-ray scattering for HBC (a) and corresponding d-spacing.

SEM images of HBC and HBC-OMe are presented in **Figure 4a and e**. HBC sample shows aggregates of submicron particles. In contrast, HBC-OMe (**Figure 4e**) has no distinct particle morphology. Furthermore, TEM micrograph (**Figure 4b and f**)

indicates that there are abundant defect sites along the lattice fringes originating from inconsecutive lattices (as marked by red circles), in great accordance with the highly porous defect morphologies (**Figure 4a and e**), which can provide sites for Na^+ storage.[35] The HRTEM images of HBC and HBC-OMe sample are displayed in **Figure 4c, d, g, h and Figure S3.** It was reported that the minimum d-spacing for Na intercalation is 0.37 nm,[11] which explains why traditional graphite could not be used as the anode materials for SIBs since its theoretical interlayer distance is only 0.34 nm. Obviously, both the HBC and HBC-OMe possess a desirable d-spacing of 0.39 nm and 0.42 nm, respectively, which corresponds to the (002) plane in **Figure 2a**. Such large interlayer distance could increase Na^+ insertion/extraction rate and provide more surface for higher reversible capacity, which is consistent with its excellent performance characteristics. **Figure 4 i-l** presents the energy-dispersive X-ray spectroscopy (EDS) mapping images of HBC-OMe sample, which shows homogeneously distributed carbon, nitrogen and oxygen elements.
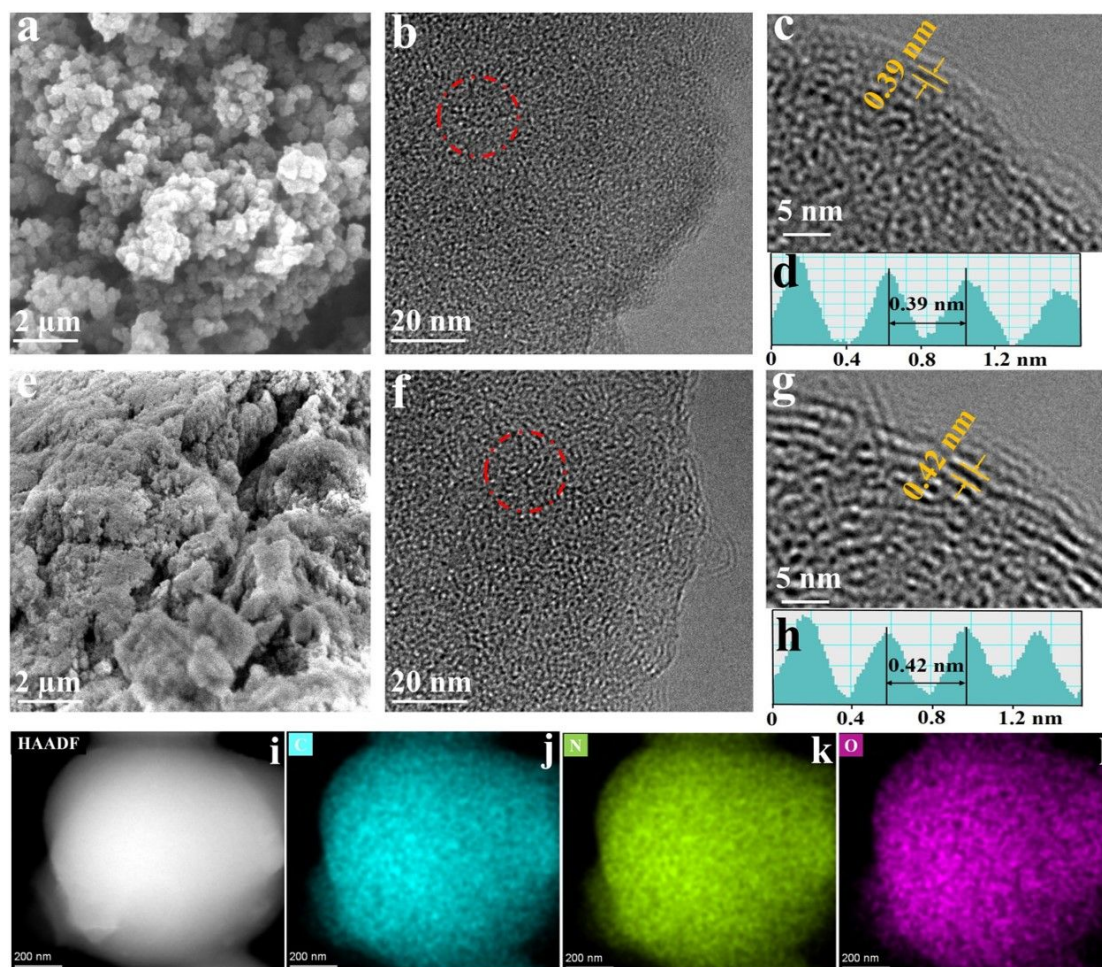
Figure 4. Morphological characterization of HBC (a-d) and HBC-OMe (e-h) samples: (a, e) SEM images, (b, f) TEM images, (c, g) HRTEM images, (d, h) intensity line plot perpendicular to the d-spacing layers and (i-l) HADDF-STEM micrograph and corresponding EDS mapping images of HBC-OMe.

The rate performances of HBC and HBC-OMe samples were acquired by cycling the electrodes at a sequent current density from 0.1 to 10 A g^{-1} within the voltage scope of 0.01 V-3.0 V. As shown in **Figure 5a**, HBC-OMe electrode present a superior rate capability than HBC, primarily because the introduction of oxygen-containing functional group which increase the Na$^+$ active sites for higher capacity. Specifically, HBC-OMe electrode delivers an amazing initial capacity of 506 mAh g^{-1} at 0.1 A g^{-1}, which outperforms most of the reported graphene-based electrodes for SIBs[36-44]

(**Figure 5b and Table S2, Supporting Information**). The corresponding average

capacity for HBC-OMe under the current densities of 0.2, 0.5, 1, 2, and 5 A g^{-1} are 425,

405, 342, 290, and 217 mAh g^{-1}, respectively, which is higher than that of 315, 275,

255, 224, 190 and 145 mAh g^{-1} for HBC electrode. Even at a high current density of 10

A g^{-1}, an excellent reversible capacity of 161 mAh g^{-1} can still be obtained. As expected,

when the current density returns to 0.1 A g^{-1}, the reversible capacity can recover to

initial state, suggesting the admirable structural stability. The long-term cycling

capability comparison of HBC and HBC-OMe electrodes are displayed in **Figure 5c-**

d. HBC-OMe electrode exhibits high initial capacity around 290 mAh g^{-1} and 217 mAh

g^{-1} at 2 A g^{-1} and 5 A g^{-1}, respectively. HBC electrode also shows excellent durability

but relatively low capacity around 195 and 140 mAh g^{-1} at respective current density.

No obvious capacity fade could be noticed throughout the whole cycling process.

Interestingly, the specific capacities seem gradually increasing from the 100th cycle to

1000th cycle. The capacity fluctuation is a commonly observed phenomenon in organic

systems, which attributed to the decomposition of electrolyte, structure evolution with time,

and temperature factor. The decomposition of electrolyte usually appears during the initial

cycles, which results in the increase of capacity but will be back to normal soon once the

decomposition finished. Structure collapse is the most common reason for the capacity

fluctuation, which would give rise to the irreversible capacity loss during the long-term

processes. However, in this paper, the capacity fluctuated all the time from 100th cycle to 1000th

cycles, Our result is similar to previously reported by Koratkar's [45] and Cao's group[46] which

shows, after an initial loss of capacity, the hierarchical nanosheet structure undergoes a volume

expansion, as is observed in graphic anode. Furthermore, nano-scaled HPB-COOH has a

smaller diffusion length, fast mass transport, and minimized polarization effects. As the cell

cycle increased, electrolyte wettability is also enhanced which allows exposure of more active

sites for intercalation. All the above factors lead to increased capacity as a function of time.
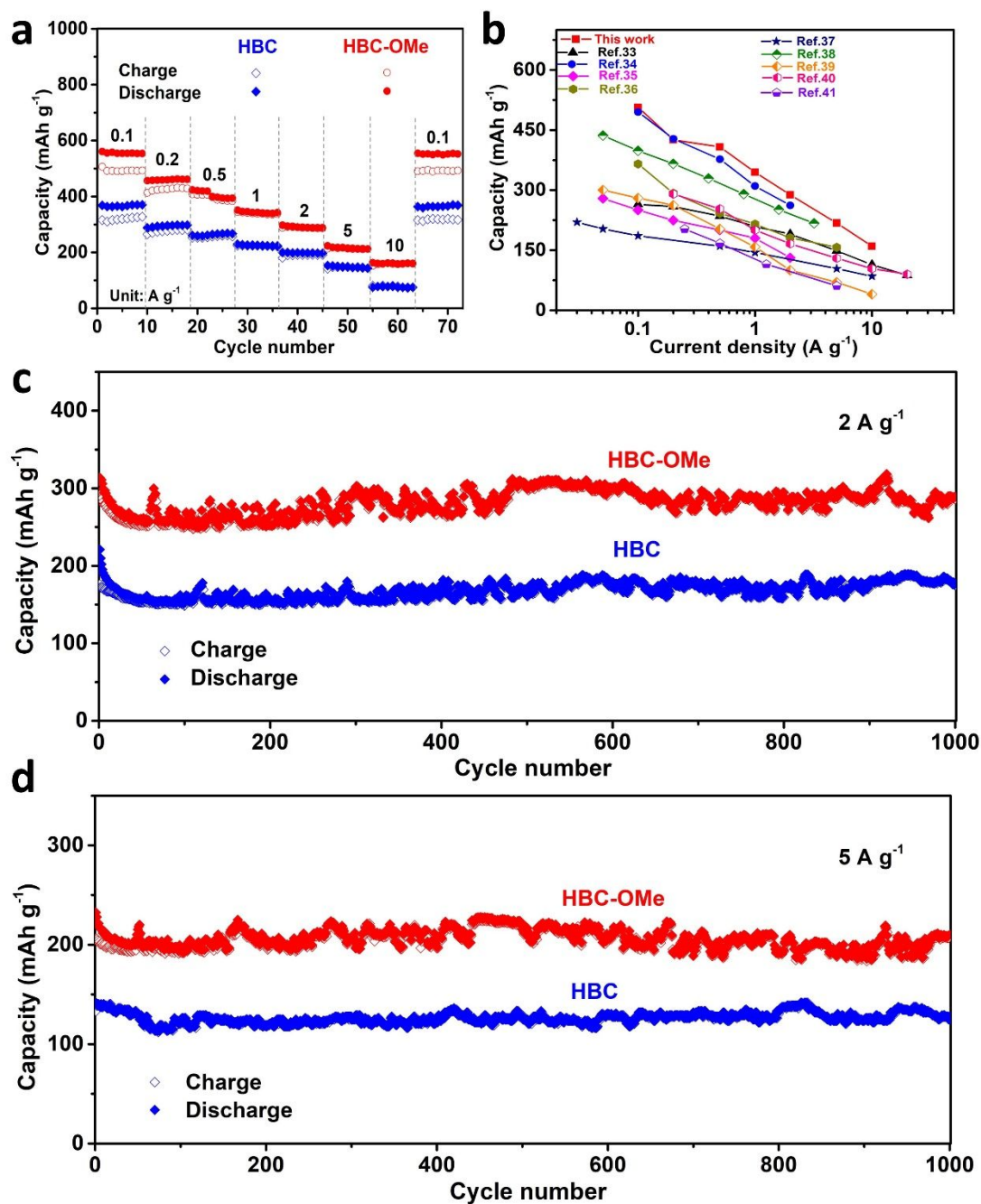
Figure 5. Electrochemical performances of as-prepared electrodes: (a) rate capabilities at different current densities, (b) rate performances comparison between HBC-OMe electrode and some representative carbon electrodes in the literature, the long-term cycling performance of HBC and HBC-OMe electrodes at a current density of 2 A g^{-1} (c) and 5 A g^{-1} (d).

The electrochemical properties associated with sodium storage of as-synthesized samples were studied by cyclic voltammetry (CV) and the Galvanostatic discharge-charge (GDC) tests. The initial four CVs of HBC at a scan rate of 0.2 mV s^{-1} within a voltage scope of 0.01-3.0 V were shown in **Figure 6a**. In the first negative scan shows a cathodic peak at around 0.9 V and nearly disappeared in the subsequent cycles, which could be ascribed to the irreversible sodium sodiation process into defects of HBC or some side reactions between Na$^+$ and surface functional groups.[40] Another weak reduction peak also appears around 0.5 V in the initial negative scan, owing to the decomposition of electrolyte and the solid-electrolyte-interface (SEI) layer formation.[41,42] After the first cycle, the highly reversible CV curves imply excellent cycling performance. The HBC-OMe display similar electrochemical behavior, as shown in **Figure 6b**, analogous cathodic peaks could also be observed in the first negative scan, however, it has a stronger reduction peak ~0.5 V compared with that in **Figure 6a**, which suggests that the HBC-OMe sample is prone to form SEI film for the initial discharging process. GDC tests were performed to further investigate the performances of the battery, **Figure 6c** shows the initial GDC tests of HBC sample at a current density of 0.1 A g^{-1}, the first discharge and charge capacities are 1856.4 and 326.1 mAh g^{-1}, respectively; such a large-capacity loss for the initial cycle is attributed

to the SEI formation resulting from side reaction and electrolyte degradation. In addition, according to the HRTEM images in Figure 4 b and f in manuscript, there exists abundant defects and irregular structures in both HBC and HBC-OMe samples. A large number of Na^+ could intercalate these inconsecutive defects and edges and thus obtain a high capacity. However, this process is normally irreversible since the intercalation of sodium with relatively large atomic radius would result in the low kinetic and partial structure collapse, so the irreversible Na^+ intercalation is the major reason for the initial low coulombic efficiency. Similarly, the HBC-OMe also shows an apparent gap between first discharge and charge capacity (**Figure 6d**), it delivers a much higher initial discharge capacity of 3120.1 mAh g^{-1} compared with that of HBC electrode. We rationalize this enhanced charge capacity is due to the introduction of oxygen-containing functional group and more defects on the surface of HBC-OMe sample.[40] Additionally, during the initial cycles, the capacity loss for HBC-OMe is greater than for HBC (inset of Figure 6c, d), which can be attributed to the difference in the structure/composition of SEI film.[47,48]
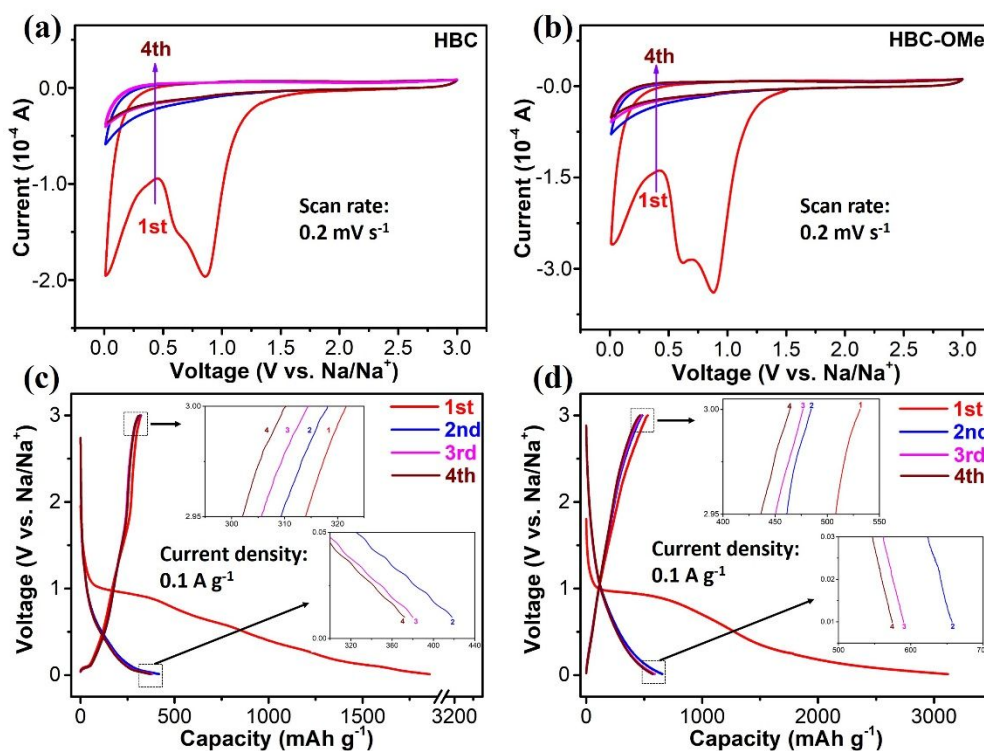
Figure 6. Cyclic voltammetry (CV) curves of HBC (a) and HBC-OMe (b); Galvanostatic discharge-charge (GDC) plots of HBC (c) and HBC-OMe (d).

To investigate the influence of Na$^+$ intercalation processes on the as-prepared samples' morphologies, the SEM test for the extensively cycled HBC and HBC-OMe anodes were carried out. Compared with the disordered and irregular morphologies as shown in **Figure 4a, e**, there is a thin film evenly forming on the surface particles after 70 charging-discharging cycles (**Figure 7a-b**), which may be originated from the side reactions between active materials and electrolytes. Although such dense structure could slightly impede the Na$^+$ diffusion and thus result in the capacity decay, it can also be regarded as the pillar protective layer to keep the electrodes' structure stability during the long-term cycling processes.

The XRD patterns for the fully cycled HBC and HBC-OMe anodes were displayed in **Figure 7c-d**. Apart from the Cu foil diffraction peak at around 43°, there is no any other noticeable impurities, which demonstrates the excellent structural stability during Na^+ intercalation processes. However, compared to the pristine sample, the major diffraction peak (around 22°) for electrode after 70th cycles became broader. When cycled to 110th, this peak became further broader, suggesting a relax in crystal structure resulting from the volume change due to the continuously intercalation processes of relatively larger Na^+. Despite the increasingly broader major peak, its position remains. To obtain more detailed structural information after the continuous charging/discharging cycles, the Raman spectrum measurements for the fully cycled electrodes HBC and HBC-OMe were carried out. As shown in **Figure 7e-f**, after 100 cycles, the I_D/I_G ratio of both HBC and HBC-OMe sample increased from 0.60 and 0.82 to 0.92 and 0.97, respectively. The increase of defect peak (I_D) intensity suggests that structure has underwent changes in molecular level in order to accommodate greater number of Na^+.
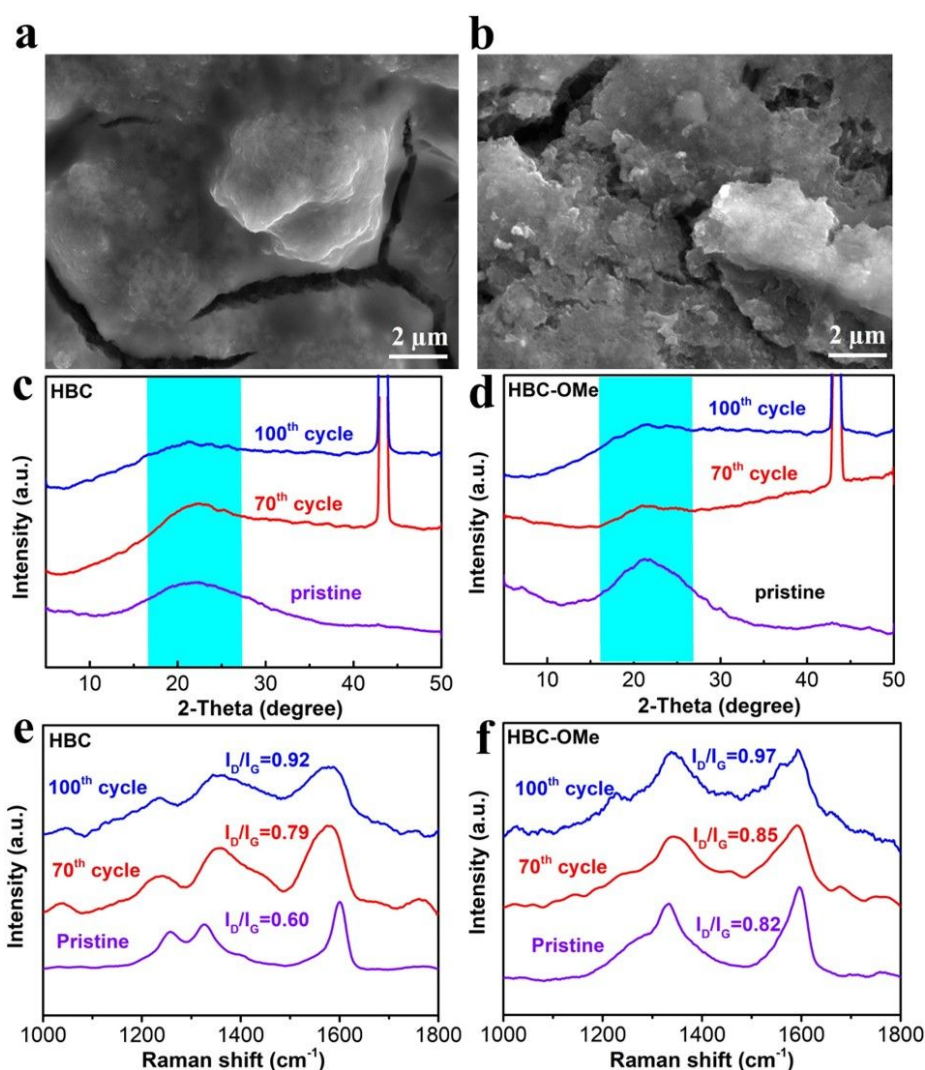
Figure 7. SEM images of the 70th cycled sample HBC (a) and HBC-OMe (b); The pristine and fully cycled XRD patterns (c-d) and Raman spectrum (e-f). Current density: 0.2 A g^{-1}.

The Na^{+} storage kinetics performances of two electrodes were analyzed by plotting CV curves at different scan rates (**Figure S4 a, c**). For most carbonaceous electrodes,[49,50] both the diffusion-controlled intercalation process (DIP) and surface-induced capacitive process (SCP) contribute to the overall charge capacity. Such mixed storage mechanism can be quantitively analyzed according to the equation $i = av^b$, where i is the redox current and v is the corresponding scan rate, a and b are constants. The b-value plays an important role in determining which process is predominant. Specifically,

the absolute DIP and SCP should be indicated by the index of 0.5 and 1, respectively.

As shown in **Figure S4 b, d**, the *b*-value for HBC and HBC-OMe is 0.84 and 0.85,

respectively, suggesting the sodium storage is mainly resulted from the SCP. Compared

with apparent peaks resulted from the interaction process in the CV curves, the surface-

induced capacitive process tends to result in much smoother CV curves, which tends to

be more kinetically facile and less structurally destructive. Sodium can intercalate the

available space between the carbon layers or can be adsorbed on the carbon surface and

even interact with functional groups.[51] Furthermore, by determining k_1 and k_2 based

on the equation $i(V) = k_1v+k_2v^{1/2}$ (where *V* and *v* represent a specific potential and scan

rate, respectively, k_1 and k_2 are constants), the current arising from the SCP (k_1v) and

that from the DIP under a fixed potential could be quantitively separated.[51] As shown

in **Figure 8 a,c**, it is clear that the capacitive contribution ratio of two electrodes

presents an increasing trend with faster scan rate. Initially, under a relatively low scan

rate of 0.2 mV s^{-1}, the capacitive contribution for both HBC and HBC-OMe electrode

are below 50% (45% and 43%, respectively), indicating Na$^+$ diffusion-controlled

processes provide more capacity when the scan rate is enough low. When increasing

the scan rate to 0.4 mV s^{-1}, the insertion and capacitive processes contributed equally

for the total capacity. Eventually, with the continuously increasing scan rate, the

capacitive contribution of HBC and HBC-OMe electrodes overwhelmingly stands out

compared with the Na$^+$ diffusion contribution, SCP contribution rise to around 85% at

a scan rate of 3 mV s^{-1} (**Figure 8 b-d**) and continuously climb to 93% under a high scan

rate of 4 mV s^{-1}. Such a dramatic increase of capacitive contribution with the increasing

scan rate indicates that the total capacity at a high scan rate is largely originated from

the SCP. Compared with bulk intercalation which is normally associated with volume

expansion during sodiation process, SCP tends to be more kinetically facile and less

structurally destructive. Electrochemical impedance spectroscopy (EIS) technique was

used to investigate the kinetic performances during electrochemical desodiation process.

As shown in **Figure S5**, the Nyquist profiles are comprised of two different regions,

one is semicircle located in the high-medium frequency range, which is associated to

the charge-transfer resistance (*Rct*), and the other straight line in the low frequency

region is ascribed to the Na$^+$ diffusion in the electrode. For HBC electrodes, obviously,

compared with the pristine electrode, the diameter of the semicircle increased rapidly

when discharged to 0.5 V and slowly decreased when discharged to 0.01 V, indicating

the speedy increasing *Rct* during discharging process, which could be originated from

the SEI film formation and the electrolyte activation, in great agreement with the above

CV and GDC results. The *Rct* apparently declined during charging process, which

demonstrates that the SEI layer has been gradually stable until the end the first

discharging process. The *Rct* of HBC-OMe electrodes display similar change trend

during different charging and discharging states. Interestingly, when charged to 3.0 V,

the *Rct* of HBC-OMe electrode is much smaller than that of HBC electrode, implying

a higher electrical conductivity, which is consistent with rate capability.
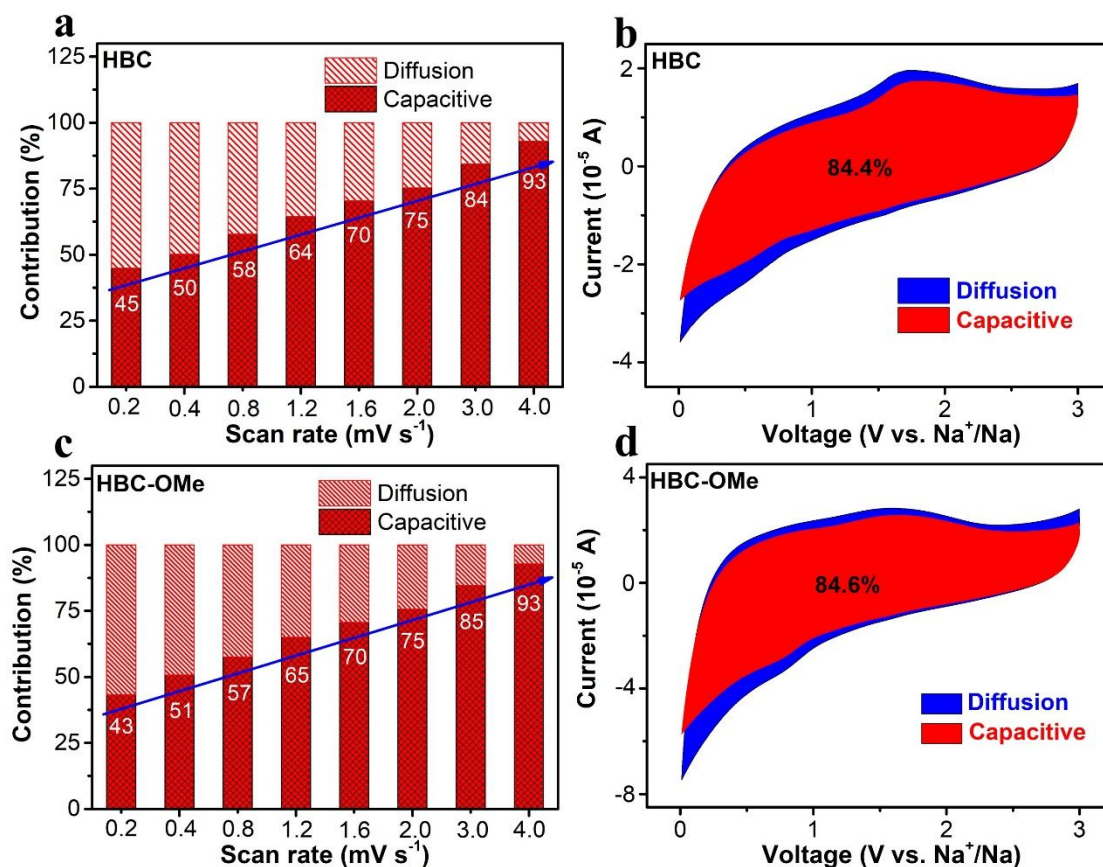
Figure 8. Electrochemical kinetics analysis of the electrodes. (a, c) Normalized contribution percentages for HBC and HBC-OMe tested at the scan rates from 0.2 to 4.0 mV s^{-1}, (b, d) CV curves of HBC and HBC-OMe electrodes with the capacitive contribution at a scan rate of 3.0 mV s^{-1}.

4. Conclusion

In summary, a novel synthesized organic molecule HBC and corresponding derivate HBC-OMe was perfectly applied in Na$^+$ storage. Particularly, the oxygen-contained HBC-OMe electrode delivers admirable sodium storage capability, attaining a high capacity of 506 mAh g^{-1} at 0.1 A g^{-1}, excellent rate capability (217 mAh g^{-1} at 5 A g^{-1}) and superior long-term durability (290 mAh g^{-1} at 2 A g^{-1} with ≈100% capacity retention after 1000 cycles). The remarkable performances are largely attributed to the 3D self-assembled hierarchical structure, which is validated by the GISAXS analysis.

In addition, surface-dominant capacitive process tends to be more kinetically facile and less structurally destructive during long-term cycling compared with diffusion-controlled intercalation process. This novel design of 3D self-assembled structure with HBC-OMe anode for SIBs presents significantly desirable sodium storage capability, providing innovative insights for design of high-performance electrodes for SIBs.

Acknowledgements

References

[1] J. B. Goodenough, K.-S. Park, *J. Am. Chem. Soc.* **2013**, *135*, 1167.

[2] C. Chen, Y. Wen, X. Hu, X. Ji, M. Yan, L. Mai, P. Hu, B. Shan, Y. Huang, *Nat. Commun.* **2015**, *6*, 6929.

[3] D. Larcher, J. M. Tarascon, *Nat. Chem.* **2015**, *7*, 19.

[4] M. Armand, J.-M. Tarascon, *Nature.* **2008**, *451*, 652.

[5] J. Y. Hwang, S. T. Myung, Y. K. Sun, *Chem. Soc. Rev.* **2017**, *46*, 3529.

[6] G. L. Xu, R. Amine, A. Abouimrane, H. Che, M. Dahbi, Z. F. Ma, I. Saadoune, J. Alami, W. L. Mattis, F. Pan, Z. Chen, K. Amine, *Adv. Energy Mater.* **2018**, *8*, 1702403.

[7] J. Qu, T. Sheng, Z. G. Wu, T. R. Chen, H. Chen, Z. G. Yang, X. D. Guo, J. T. Li, B. H. Zhong, S. X. Dou, *J. Mater. Chem. A.* **2018**, *6*, 13934.

[8] L. Li, Y. Zheng, S. Zhang, J. Yang, Z. Shao, Z. Guo, *Energy Environ. Sci.* **2018**, *11*, 2310.

[9] P. Barpanda, L. Lander, S.-I. Nishimura, A. Yamada, *Adv. Energy Mater.* **2018**, *8*, 1703055.

[10] J. Qu, D. Wang, Z. G. Yang, Z. G. Wu, L. Qiu, X. D. Guo, J. T. Li, B. H. Zhong, X. C. Chen, S. X. Dou, *ACS Appl. Mater. Interfaces*, **2019**, *11*, 26938.

[11] Y. Xiao, N. M. Abbasi, Y. F. Zhu, S. Li, S. J. Tan, W. Ling, L. Peng, T. Q. Yang, L. Wang, X. D. Guo, Y. X. Yin, H. Zhang, Y. G. Guo, *Adv. Funct. Mater.* **2020**, 2001334.

[12] Y. Xiao, Y. F. Zhu, W. Xiang, Z. G. Wu, Y. C. Li, J. Lai, S. Li, E. H. Wang, Z. G. Yang, C. L. Xu, B. H. Zhong, X. D. Guo, *Angew. Chem. Int. Ed.* **2020**, *59*, 1491.

[13] Y. F. Zhu, Y. Xiao, W. B. Hua, S. Indris, S. X. Dou, Y. G. Guo, S. L. Chou, *Angew. Chem. Int. Ed.* **2020**, *132*, 1.

[14] Z. Z. Zhang, Y. C. Du, Q. C. Wang, J. Y. Xu, Y. N. Zhou, J. C. Bao, J. Shen, X. S. Zhou. *Angew. Chem. Int. Ed.* **2020**, *59*, 17504−17510

[15] Z. F. Liu. Insight into Effects of Fluoroethylene Carbonate Additive on the Cathode in Sodium Ion Batteries. *Acta Physico-Chimica Sinica.* **2019**, *35*, 804−805.

[16] J. Y. Xu, E. L. Gu, Z. Z. Zhang, Z. H. Xu, Y. F. Xu, Y. C. Du, X. S. Zhu, X. S. Zhou. *J. Colloid Interface Sci.* **2020**, *567*, 84−91.

[17] M. M. Song, C. C. Wang, D. F. Du, F. J. Li, J. Chen. *China Chem*. **2019**, 62, 616−621.

[18] Y. Wen, K. He, Y. Zhu, F. Han, Y. Xu, I. Matsuda, Y. Ishii, J. Cumings, C. Wang, *Nat. Commun.* **2014**, *5*, 4033.

[19] Z. L. Xu, G. Yoon, K. Y. Park, H. Park, O. Tamwattana, S. Joo Kim, W. M. Seong, K. Kang, *Nat. Commun.* **2019**, *10*, 2598.

[20] X. F. Luo, C. H. Yang, Y. Y. Peng, N. W. Pu, M. D. G, C. T. Hsieh, J. K. Chang, *J. Mater. Chem. A.* **2015**, *3*, 10320.

[21] J. Zhao, Y. Z. Zhang, J. Y. Chen, W. L. Zhang, D. Y, R. Chua, H. N. Alshareef, Y. W. Ma, *Adv. Energy Mater.* **2020**, *10*, 2000099.

[22] Z. Che, Y. Li, K. Chen, M. Wei, *J. Power Sources* **2016**, *331*, 50.

[23] G. Wang, J. Zhang, S. Yang, F. Wang, X. Zhuang, K. Müllen, X. Feng, *Adv. Energy Mater.* **2018**, *8*, 1702254.

[24] A. T. Lawal, P. Fantke, *Cogent Environmental Science*, **2017**, *3*, 1.

[25] A. K. Haritash, C. P. Kaushik, *J Hazard Mater*, **2009**, *169*, 1.

[26] M. Miroshnikov, K. P. Divya, G. Babu et al, *J. Mater. Chem. A.* **2016**, *4*, 12370.

[27] H. J. Yen, H. Tsai, M. Zhou, E. F. Holby, S. Choudhury, A. Chen, L. Adamska, S. Tretiak, T. Sanchez, S. Lyer, H. G. Zhang, L. X. Zhu, H. Q. Lin, L. M. Dai, G. Wu, H. L. Wang, *Adv. Mater.* **2016**, *28*, 10250.

[28] D.W. Wang, C. H. Sun, G. M. Zhou, F. Li, L. W, B. C. Donose, G. Q. Lu, H. M. Cheng, L. R. Gentle, *J. Mater. Chem. A.* **2013**, *1*, 3607.

[29] E. Yoo, J. Kim, E. Hosono, H. Zhou, T. Kudo, I. Honma, *Nano letter*, **2008**, *8*, 2277.

[30] Y. Y. Liu, V. I. Artyukhov, M. J. Liu, A. R. Harutyunyan, B. I. Yakobson, *Physical Chemistry Letters*, **2013**, *4*, 1737-1742.

[31] J. Zhao, Y. Z. Zhang, F. Zhang, H. F. Liang, F. W. Ming, H. N. Alshareef, Z. Q. Ga, *Adv. Energy Mater.* **2019**, *9*, 1803215.

[32] E. B. Mclean, V. Gauchot, S. Brunen, D. J. Burns, A. L. Lee, *Chemical Communication,* **2019**, *55*, 4238-4241.

[33] K. Krishnamoorthy, M. Veerapandian, K. Yun, S. Kim, *Carbon* **2013**, *53*, 38.

[34] J. Rivnay, S. C. B. Mannsfeld, C. E. Miller, A. Salleo, M. F. Toney, *Chem. Rev.* **2012**, *110*, 3.

[35] Z. Li, Y. Chen, Z. Jian, H. Jiang, J. J. Razink, W. F. Stickle, J. C. Neuefeind, X. Ji, *Chem. Mater.* **2018**, *30*, 4536.

[36] D. Datta, J. Li, V. B. Shenoy, *ACS Appl. Mater. Interfaces* **2014**, *6*, 1788.

[37] J. L. Liu, Y. Q. Zhang, L. Zhang, F. X. Xie, A. Vasileff, S. Z. Qiao, *Adv. Mater.* **2019**, *31*, 1901261.

[38] Y. Yang, Z. Z. Pan, Y. Y. Wang, Y. C. Ma, C. L, Y. J. Lu, X. L. Wu, *Nanoscale*. **2019**, *11*, 14616.

[39] M. M. Kang, H. Q. Zhao, J. Q. Ye, W. Song, H. T. Shen, J. Mi, Z. Li, *J. Mater. Chem. A*, **2019**, *7*, 7565.

[40] X. F. Luo, C. H. Yang, J. K. Chang, *J. Mater. Chem. A*, **2015,** *3*, 17282.

[41] B. Quan, A. Jin, S. H. Yu, S. K. Kang, J. Jeong, H. D. Abruna, L. Y. Jin, Y. Z. Piao, Y. E. Sung, *Adv. Sci.* **2018**, *5*, 1700880.

[42] N. Sun, Y. B. Guan, Y. T. Liu, Q. Z. Zhu, J. R. Shen, H. Liu, S. Q. Zhou, B. Xu, *Carbon*. **2018**, *137*, 475.

[43] H. S. Hou, C. E. Banks, M. J. Jing, Y. Zhang, X. B. Ji, *Adv. Mater.* **2015**, *27*, 7861.

[44] Z. F. Li, Z. L. Jian, X. F. Wang, I. A. Rodri´guez-Pe´rez, *Chem. Commun.* 2017, *53*, 2610.

[45] R. Mukherjee, A. V. Thomas, D. Datta, E. Singh, J. Li, O. Eksik, V. B. Shenoy, N. Koratkar, *Nature Communications*. **2014**, *5*, 3710.

[46] J. H. Hou, C. B. Cao, F. Ldrees, X. L. Ma, *ACS Nano*. **2015**, *9*, 2556-2564.

[47] B. Lee, M. Kim, S. Kim, L. Nanda, S. J. Kwon, H. D. Jang, D. Mitlin, S. W. Lee, *Adv. Energy Mater.* **2020**, *10*, 1903280.

[48] L. Fu, K. Tang, K. Song, P. A. van Aken, Y. Yu, J. Maier, *Nanoscale.* **2014**, *6*, 1384.

[49] K. Tang, L. Fu, R. J. White, L. Yu, M. M. Titirici, M. Antonietti, J. Maier, *Adv. Energy Mater.* **2012**, *2*, 873.

[50] H. Wang, Z. Wu, F. Meng, D. Ma, X. Huang, L. Wang, X. Zhang, *ChemSusChem* **2013**, *6*, 56.

[51] D. Xu, C. Chen, J. Xie, B. Zhang, L. Miao, J. Cai, Y. Huang, L. Zhang, *Adv. Energy Mater.* **2016**, *6*, 1501929.